

The ZEPLIN-III dark matter detector: instrument design, manufacture and commissioning

D. Yu. Akimov^a, G. J. Alner^b, H. M. Araújo^{c,b}, A. Bewick^c,
C. Bungau^{c,b}, A. A. Burenkov^a, M. J. Carson^d, V. Chepel^e,
D. Cline^f, D. Davidge^c, J. C. Davies^d, E. Daw^d, J. Dawson^c,
T. Durkin^b, B. Edwards^{c,b}, T. Gamble^d, C. Ghag^g,
R. J. Hollingworth^d, A. S. Howard^c, W. G. Jones^c, M. Joshi^c,
J. Kirkpatrick^d, A. Kovalenko^a, V. A. Kudryavtsev^d,
I. S. Kuznetsov^a, T. Lawson^d, V. N. Lebedenko^c, J. D. Lewin^b,
P. Lightfoot^d, A. Lindote^e, I. Liubarsky^c, M. I. Lopes^e,
R. Lüscher^b, J. E. McMillan^d, B. Morgan^d, D. Muna^d,
A. S. Murphy^g, F. Neves^e, G. G. Nicklin^d, S. M. Paling^d,
D. Muna^d, J. Pinto da Cunha^e, S. J. S. Plank^g, R. Preece^b,
J. J. Quenby^c, M. Robinson^d, C. Silva^e, V. N. Solovov^e,
N. J. T. Smith^b, P. F. Smith^b, N. J. C. Spooner^d,
V. Stekhanov^a, T. J. Sumner^{c,*}, C. Thorne^c, D. R. Tovey^d,
E. Tziaferi^d, R. J. Walker^c, H. Wang^f, J. White^h & F. Wolfsⁱ

^a*Institute for Theoretical and Experimental Physics, Moscow, Russia*

^b*Particle Physics Department, Rutherford Appleton Laboratory, Chilton, UK*

^c*Blackett Laboratory, Imperial College London, UK*

^d*Physics and Astronomy Department, University of Sheffield, UK*

^e*LIP-Coimbra & Department of Physics of the University of Coimbra, Portugal*

^f*Department of Physics & Astronomy, University of California, Los Angeles, USA*

^g*School of Physics, University of Edinburgh, UK*

^h*Texas A&M University, USA*

ⁱ*University of Rochester, New York, USA*

Abstract

We present details of the technical design and manufacture of the ZEPLIN-III dark matter experiment. ZEPLIN-III is a two-phase xenon detector which measures both the scintillation light and the ionisation charge generated in the liquid by interacting particles and radiation. The instrument design is driven by both the physics requirements and by the technology requirements surrounding the use of liquid xenon. These include considerations of key performance parameters, such as the efficiency of scintillation light collection, restrictions placed on the use of materials to control the inherent radioactivity levels, attainment of high vacuum levels and chemical contamination control. The successful solution has involved a number of novel design and manufacturing features which will be of specific use to future generations of direct dark matter search experiments as they struggle with similar and progressively more demanding requirements.

Key words: ZEPLIN-III, dark matter, liquid xenon, radiation detectors, WIMPs
PACS: code, code

1 Introduction

ZEPLIN-III is a two-phase (liquid/gas) xenon detector developed and built by the ZEPLIN Collaboration,¹ which will try to identify and measure galactic dark matter in the form of Weakly Interacting Massive Particles, or WIMPs [1,2]. Upon completion of physics testing now underway at Imperial College, the system will join the ZEPLIN-II [3] and DRIFT-IIa [4] experiments already operating 1100 m underground in our laboratory at the Boulby mine (North Yorkshire, UK).

Two-phase emission detectors based on the noble gases date back several decades [5]. In last decade, this technology has gained a new momentum in view of increasing interest for searching rare events, WIMPs in particular, requiring both large detection masses and high discrimination against background. In its previous work, the ZEPLIN Collaboration has explored the potential of high-field xenon systems to enhance sensitivity and background discrimination [6,7,8]. The operating principle relies on different particle species

* Corresponding author; address: Astrophysics Group, Blackett Laboratory, Imperial College London, SW7 2BW, UK

Email address: t.sumner@imperial.ac.uk (T. J. Sumner).

¹ Edinburgh University, Imperial College London, ITEP-Moscow, LIP-Coimbra, Rochester University, CCLRC Rutherford Appleton Laboratory, Sheffield University, Texas A&M, UCLA.

generating different amounts of vacuum ultra-violet (VUV) scintillation light and ionisation charge in liquid xenon (LXe). The ratio between these two signal channels provides a powerful technique to discriminate between electron and nuclear recoil interactions. WIMPs are expected to scatter elastically off Xe atoms, much like neutrons, and the recoiling nucleus will produce a different signature to γ -ray interactions and other sources of electron recoils.

WIMP detectors differ from more traditional detectors of nuclear radiation in that they require: i) extremely low radioactive and cosmic-ray backgrounds, addressed by the use of radio-pure materials and operation deep underground; ii) excellent discrimination of the remaining background events, especially for electron recoils; iii) a low energy threshold for nuclear recoils, since the kinematics of WIMP-nucleus scattering results in a very soft recoil spectrum ($\lesssim 100$ keV).

Monte Carlo simulations [9,10] were essential in key areas to inform the design of the instrument. Acceptable levels of trace contamination must be set for all detector materials, requiring simulations of internal and external backgrounds expected from each component. Cosmic-ray-induced backgrounds also need careful calculation, since experimental measurements would require nothing short of a dedicated WIMP detector. These simulations establish the residual electron/photon and neutron event rates and spectra. Detailed detector simulations leading to predicted data timelines can be used to find the level of discrimination and energy threshold which can realistically be achieved. Feedback from this process into the design process has been essential for ZEPLIN III. In addition, the data produced by two-phase detectors are often complex, and particular simulations are required to help extract actual physics parameters. Finally, realistic datasets help with planning the data acquisition electronics and the data analysis software.

In this paper we describe the instrument design philosophy, the engineering design solutions and the manufacturing processes adopted. In a separate paper [11] we present full performance Monte Carlo simulations for the final, as built, instrument.

2 The ZEPLIN-III instrument

There are four important design requirements for a dark matter detector: a low energy threshold, good particle discrimination, 3-D position reconstruction and a low background within the fiducial volume. The ZEPLIN III approach, as shown in figure 1, tries to push the boundaries of the two-phase xenon technique to simultaneously achieve the best performance possible in these four aspects.

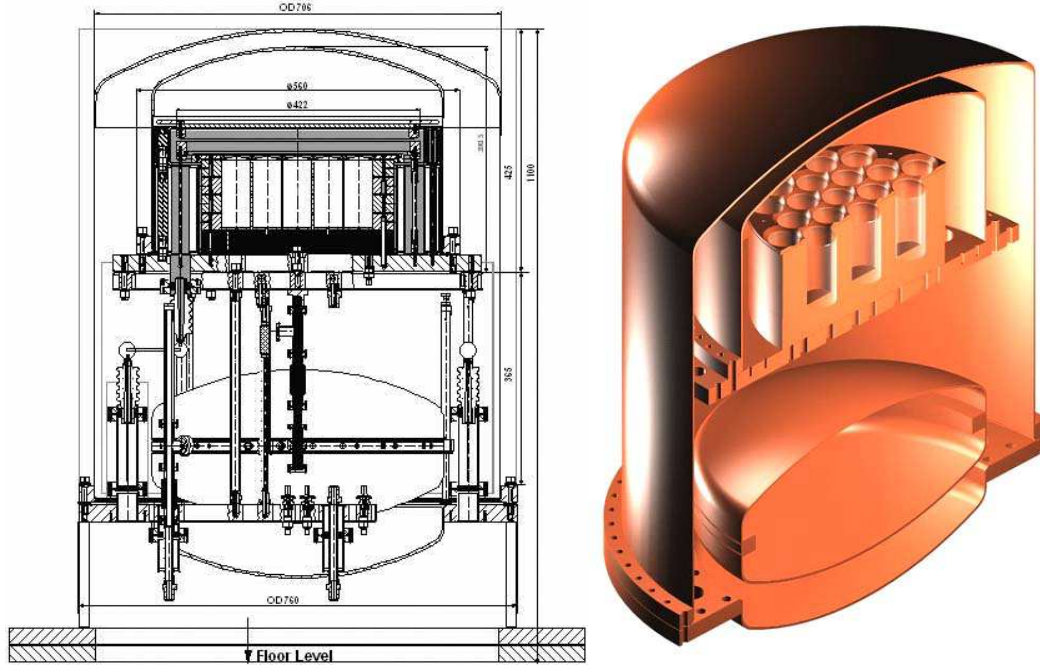


Fig. 1. Cross-sectional views of the ZEPLIN III instrument showing the key system design concepts. The rendered CAD representation shows the copper parts.

ZEPLIN-III achieves a low threshold for the primary scintillation by placing its photo-detectors, photomultipliers (PMTs) in the liquid phase and by using a flat planar geometry. Using PMTs in the liquid removes two interfaces, both with large refractive index mismatches and puts in an additional interface at which total internal reflection also works to improve the light collection for the primary scintillation. The planar geometry gives a large solid angle acceptance and lessens the dependence on surface reflectivities. A low threshold for the electroluminescence from the gas phase which provides the secondary signal is achieved by using a high electric field in the gas region to produce high levels of photon emission per electron emitted from the surface and by using refraction at the liquid surface to produce a ‘focusing’ effect for the light onto the immersed PMT array.

ZEPLIN-III achieves good particle discrimination between the nuclear recoil signals expected from WIMPs and the electron recoils from photon backgrounds by employing a two-phase design which allows both scintillation and ionisation to be measured for each event. The ratio of these two signals depends on the particle species. The effectiveness of this discrimination depends on the width and separation of the distributions for each species. It turns out [12] that the discrimination is improved by working at moderate electric fields which increases the separation between the two distributions and improves the statistical uncertainties of the ionisation signal. Some discrimination against nuclear recoil signals from neutron elastic scattering is obtained by having good 3-D position reconstruction which can identify the multiple scattering

expected from the much higher cross-sections for neutron scattering than for WIMP scattering. Efficient measurement of the ionisation relies on achieving a long lifetime against trapping for free electrons in the liquid. This requires ultra-pure xenon as free from electronegative impurities as possible. The target volumes must be constructed as high vacuum vessels and a dedicated gas purification system is needed.

ZEPLIN-III achieves good 3-D position reconstruction by using an array of 31 2" diameter photomultipliers. These provide sub-cm 2-D spatial resolution in the horizontal r, θ plane. Resolution in the z co-ordinate at the $\sim 50 \mu\text{m}$ level is obtained from the timing between the primary and secondary scintillation signals.

ZEPLIN-III achieves a low background partly by operation underground and partly by using a very restricted range of materials for its construction. Although the PMTs are the largest specific contributors to the background budget it is important that careful attention is paid to all materials used as these exceed the PMT mass by two orders of magnitude. In addition it is planned to eventually replace the PMTs by low-background versions which are currently in development.

In the following sections we detail the design and manufacture of the individual parts of the ZEPLIN III experiment. These include the target volume, the cooling system, the outer vacuum jacket, the gas handling system, including the safety reservoirs, and the data acquisition system. In the final section we provide data from surface commissioning tests which validate the key performance parameters for ZEPLIN III

3 The target volume

The detailed design of the inner components within the target volume is shown in figure 2.

3.1 The PMT array

Inside the xenon vessel is the array of 31 PMTs, immersed in the liquid phase, looking up to a $\simeq 40$ mm-thick liquid xenon layer on top of which is a 5 mm xenon gas gap. The figure shows a cross-sectional view through a centre line passing through 5 of the 52 mm diameter PMTs. The others are arranged in a hexagonal close-packed array with a pitch spacing of 54 mm. A pure copper 'screen' has an array of 53 mm holes into which the PMTs fit. This provides

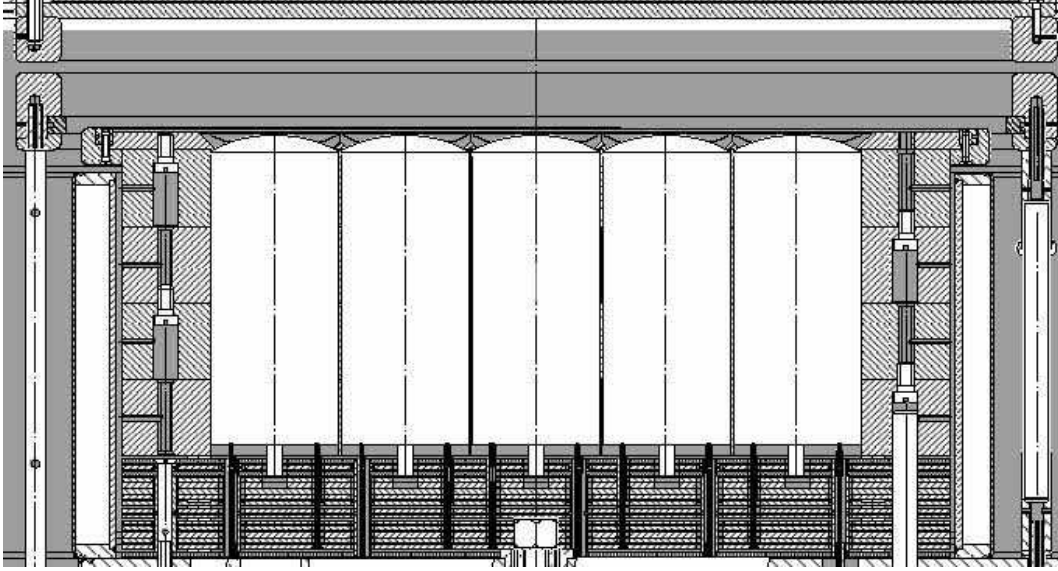


Fig. 2. Cross-sectional assembly drawing of the internal chamber volume of ZEPLIN III.

both light screening and electrical isolation between the PMTs. It has an outer diameter of 340 mm and a height of 128 mm. For ease of manufacture the total height of the ‘screen’ was made in four sections. Each PMT hole through the copper ‘screen’ has a diameter of 53mm giving a 1 mm wall minimum thickness between each PMT. Two techniques were used to produce such thin wall section through such a thickness of copper; wire erosion and boring. Both worked but the boring produced a better surface finish. Sitting directly on top of the ‘screens’ is another copper disc with holes in it. This time the thickness is 7 mm and the holes are finished with highly polished conical sections to improve the light collection; this plate is hence referred to as the ‘PMT mirror’.

Each PMT has 15 pins to which connections must be made (12 dynodes, anode, cathode and focus). However it would be impractical to bring all 465 connections out through individual UHV electrical feeds through the bottom thick copper flange. Instead all the PMTs are run from a common high voltage supply and dynode distribution system which reduces the amount of feedthroughs to just 47. The corresponding dynode pins on each PMT are connected together using a stack of 16 thin copper plates, held apart with small quartz spacers, below the PMT array. Each 2mm thick plate has a different pattern of holes (see figure 3) allowing connection to each pin in turn whilst the others pass through with clearance. Connections between the copper plates and the PMT contacts were done by first cold welding a pin into the copper plate and then using spring loaded tubes to join the two pins together (see figure 4). The pins used in the copper plates were made in copper with a gold coating and these were inserted into tight fitting holes in the plates using a drill press. The spring contacts were made from stainless steel tubing with reduced wall

sections and slots. These contacts provide enough friction for retention of the PMT against buoyancy forces during immersion in liquid xenon. Connection between each plate and its single UHV coaxial feedthrough was again made by a direct spring loaded tube but with the addition of gold-plated copper wires with silver-plated copper adaptors to provide the extensions between end contacts. The anode connection from each PMT is brought out separately on a dedicated coaxial UHV feedthrough in a similar way. The specific arrangement of the 16 copper plates can be seen in figure 4. The upper and lower plates are connected to ground. The second lowest plate is connected to the PMT cathodes, the next 11 are connected to dynodes 1 to 11 in turn. Above that there is then another grounded plate and between this and the top ground plate is dynode 12. The two grounded plates either side of the dynode 12 plate deliberately provide both extra capacitance to ground for that dynode and prevent cross-coupling with other connections. Copper tubes provide shielding along the run of each anode output connection. Shielded cables pass across the outer vacuum jacket space to connectors in its base plate. A single external voltage divider chain is used to provide all the common dynode voltages. To ensure reasonably well matched gains when running from a common HV supply, PMTs were procured with gains within prescribed limits. Once selected the batch of 35 PMTs (ETL D730/9829Q) was tested and calibrated at low temperature with Xe scintillation UV light prior to installation in the detector [13]. The PMTs were customised specifically for ZEPLIN III in two ways: firstly a conductive pattern of so-called ‘fingers’ was deposited on the inside of the window to avoid saturation at high count rates, and secondly to provide a modified pin-out arrangement to facilitate the use of the copper interconnection plates. The PMTs are operated with the cathode at ground potential.

3.2 *The electric field*

Proper operation in two-phase mode requires that there be a sufficiently high electric field in three distinct regions. In the active volume of the detector the electric field helps to separate ionisation charge released from the track of the interacting particle before it can recombine. This field must be directed such that the electrons start ‘drifting’ towards the liquid surface. Hence the field in this first region is called the ‘drift’ field. The second critical region is at the liquid/gas interface. Here the field in the liquid must be high enough to efficiently extract the electrons into the gas phase. This not only increases the signal strength but also prevents charge build-up at the surface. This field is called the ‘extraction’ field. Finally in the gas phase the field must be high enough for the accelerated electrons to produce excitation in the gas atoms. The excited atoms then form excited dimers followed by dissociative radiative emission in the usual way, which produces the signal seen by the PMTs. This

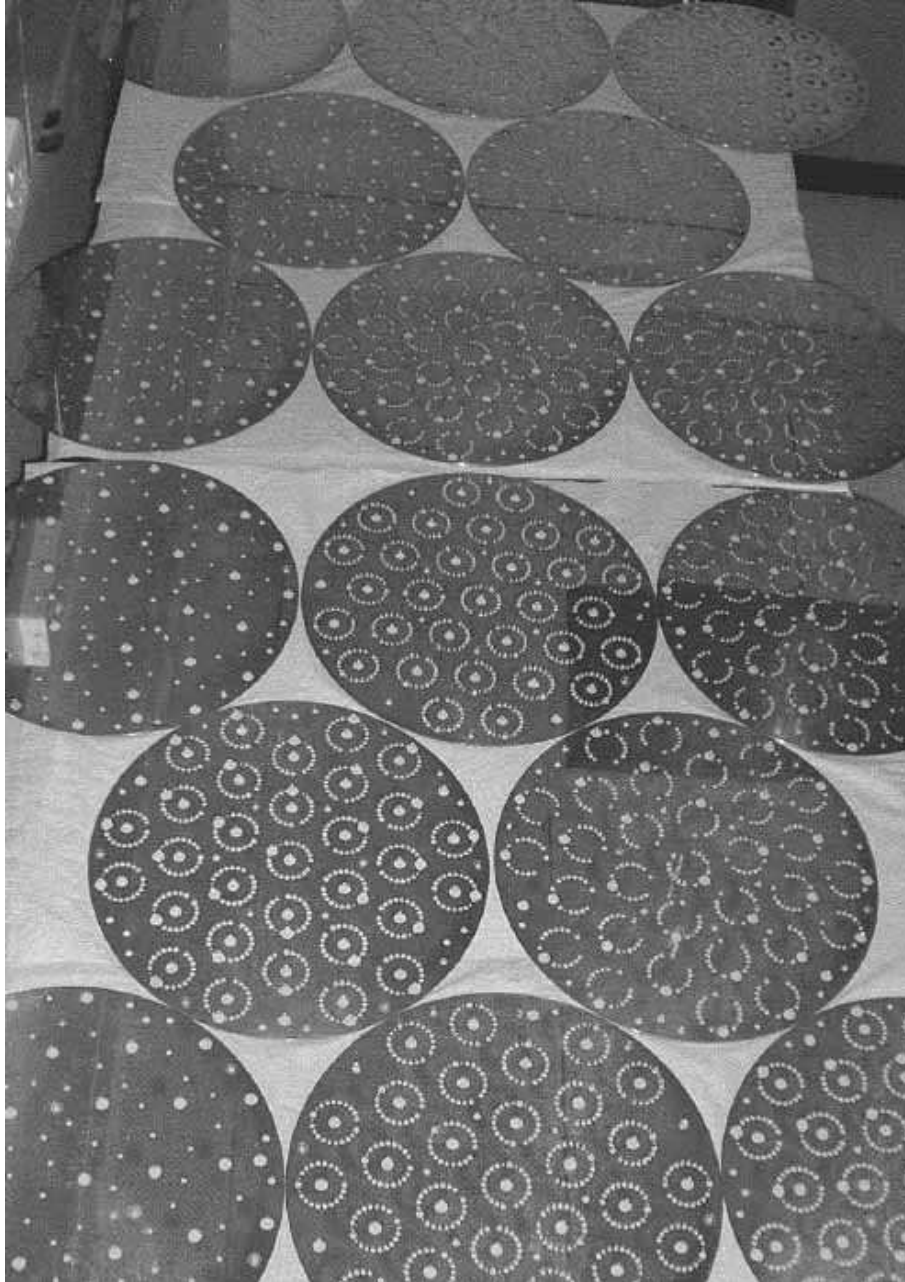


Fig. 3. The 16 2-mm copper plates used to make the internal PMT dynode interconnections.

last field is called the ‘electroluminescence’ field. These three fields can either be produced by setting up a segmented electrode structure producing distinct regions, as is done in ZEPLIN II [14], or, as in the case of ZEPLIN III, a single pair of outer electrodes can be used to produce all three at once. The advantage of the latter is the absence of any physical electrode structure in the liquid which could then be a source of background and/or feedback. However it does mean that a single much higher individual voltage is required and the fields can not be controlled independently. The two electrodes used are the

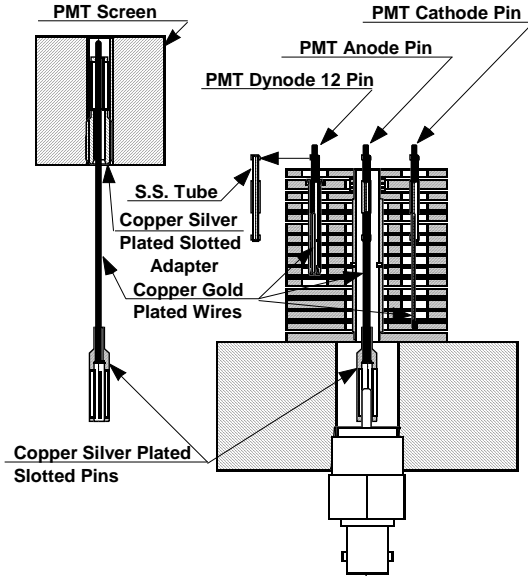


Fig. 4. Various spring loaded contacts used to connect the PMT pins to the copper plates.

solid flat plate (‘anode mirror’) above the gas gap and a wire plane (‘cathode grid’) 40 mm below it in the liquid. The 8-mm top plate is made from copper and its bottom surface has been lapped using optical techniques and left highly polished. Up to 40 kV can be applied between the two ‘electrodes’.

A second wire grid (‘PMT grid’) is located 5 mm below the cathode grid and just above the PMT array. This defines a reverse field region just above the PMTs which suppresses secondary signals from low-energy background photons from the PMTs and also helps isolate the internal PMT photocathode fields from the external high electric field. The diameter of the electrode structure is ~ 40 cm, whilst that of the PMT array is 34 cm. The fiducial volume will be defined by a combination of primary to secondary timing and position recovery from the PMT hit pattern, and it will be well inside the PMT array diameter. This ensures that the electric field will be very uniform over the fiducial volume region. Field and electron trajectory simulations, produced using ANSYS [15], are shown in figure 5.

The stainless-steel wire grids were strung from continuous lengths of $100 \mu\text{m}$ diameter wire wound around copper formers. The position of each wire was controlled by slots machined into the formers (see figure 6). The wires were tensioned using two techniques. Firstly the formers were elastically deformed whilst the wire was wound and secondly the winding jig tensioned the wire as it was wound. Once the grid winding was complete the wire was anchored and the formers were then released from their restraining jigs.

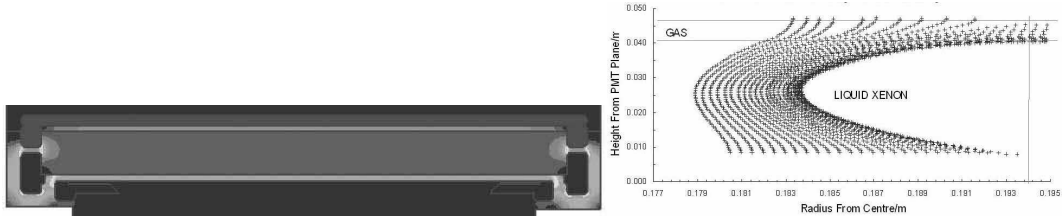


Fig. 5. Electric field distribution within the target volume as computed using ANSYS [15]. On the right is shown an expanded view of the drift paths of electrons near the right-hand gap between the two electrodes.

Some consideration was given to whether the anode mirror should be coated to enhance its reflectivity. The performance of polished copper is quite uncertain at VUV wavelengths, depending on the surface finish, oxidation state and possible LXe condensation onto the cold surface in the gas phase. Only a single measurement has been found, indicating $R=25\%$ for normal incidence for a clean-cut surface [16]. However the simplicity of leaving this surface as is, the uncertainty of using coatings in a high-field application and the desire not to compromise the spatial reconstruction argued for not using any coating.

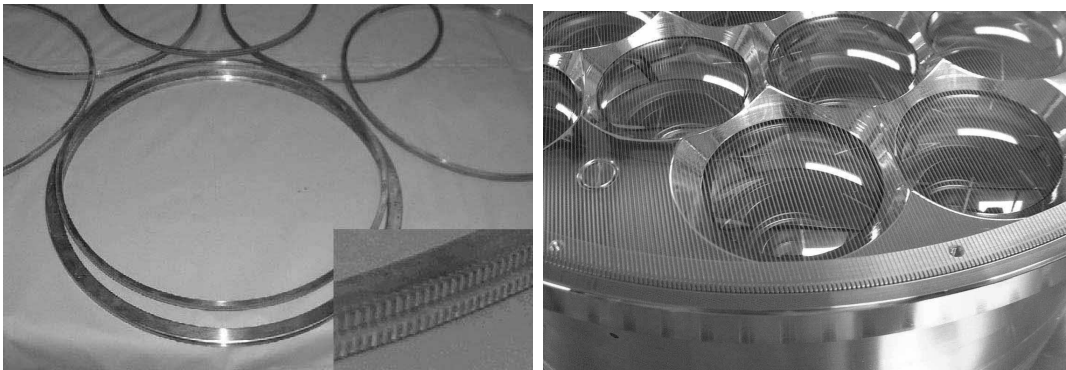


Fig. 6. On the left are the copper formers for the wire grids. The inset detail shows an expanded view in which the slots cut to control to wire positioning can be seen. On the right is a view of the assembled PMT array in which the PMT grid can be seen.

3.3 The xenon transport system

Two copper access pipes are included for movement of xenon in and out of the target vessel (see figure 7). One surfaces above the liquid level in an unconfined volume as is used as a ‘Gas Inlet’. The second has a double tube structure with an open ended inner pipe connected directly to the main xenon liquid volume, and an outer pipe which vents to the outside through the ‘LXe Outlet’. The outer pipe is sealed at the top and the inner opens above the liquid surface and essentially allows a ‘syphon’ action during emptying. Transfer of xenon in and out of the target vessel is independent of the cooling system.

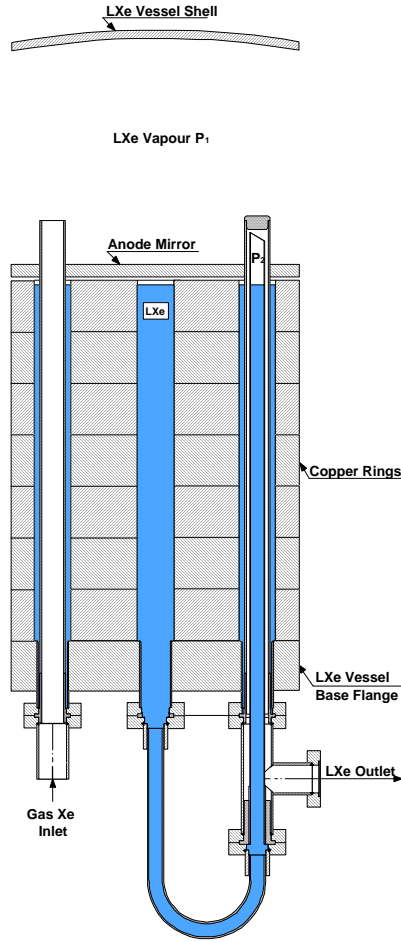


Fig. 7. Arrangement of the pipework used for xenon transfer in and out of the target vessel.

3.4 *The target vessel*

The containment vessel for the xenon target must perform as both a high vacuum vessel, for purity reasons, and a pressure vessel for safety reasons. The pressure vessel design was done following the relevant British Standard (BS5500:1997). This safety standard dictates the cylindrical wall, dome and bottom flange thicknesses which are dependent on the material and processes used. The vessel was required to be certified to 6 bar absolute. The material of choice was determined by requiring the product of total mass times radioactive content be a minimum. Added to this prime requirement was then the need for the material to be suitable for manufacture of the vessel. OFHC copper type C103 was selected. This required 4 mm wall thickness on the cylindrical sections, 3 mm for the spun domes and 25 mm for the flat bottom flange. To minimise the likelihood of inclusion of any impurities electron-beam welding was used throughout and the number of welds was kept to a minimum.

In particular the cylindrical section was rolled in one piece. Stainless steel parts were used for some specialist components which would have been very difficult to make out of copper, such as vacuum knife edge flanges and vacuum HV feedthroughs for which commercial parts were used. Where necessary these stainless parts were also electron-beam welded to the copper. Welding techniques adapted to our requirements were developed by The Welding Institute, UK[17], in close cooperation with us. This included setting the welding parameters and optimising the structural/thermal design of the weld joints. All safety critical welding was done by certified processes and copper witness plates were used to ensure proper and complete breakthrough as all welds were required to show full-depth penetration. Special jigging was required to hold all seams for welding securely in place during the process. On completion all joints were leak-tested down to the level of $\sim 10^{-10}$ mbar.l.s⁻¹.

The electrical feedthroughs for the PMT dynode connections were fitted in with screw threads with thick indium coated onto them using an ultrasonic soldering iron. The demountable vacuum seal between the cylindrical section and the bottom flange was done using a stainless steel gasket with double knife edges and an indium wire at both copper surfaces (see figure 8). All copper

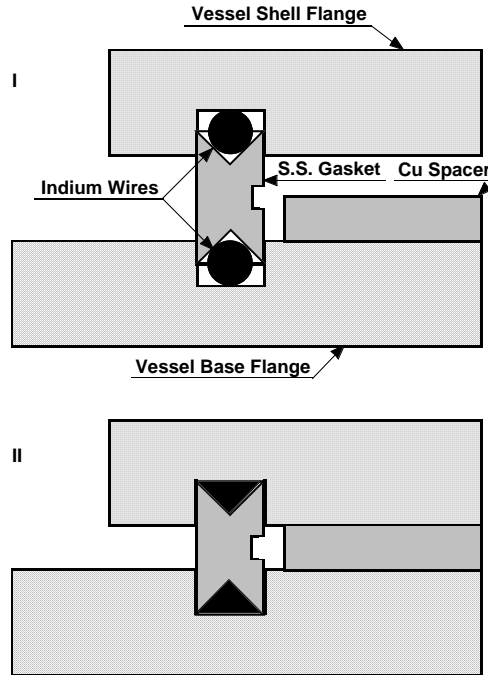


Fig. 8. Vacuum seal between the cylindrical wall section and the bottom flange before (I) and after (II) sealing.

parts were cleaned, starting with a coarse hand polishing with stainless wire wool, a fine polishing with copper wire wool, an ultrasonic bath using 2% CITRANOX [18] in de-ionised water and a high-pressure wash using pure water. The polishing phase was done using a powered rotation table specially

built for the purpose and polishing was always applied along the line of existing machining marks.

4 The cooling system

Cooling is done using liquid nitrogen (LN2). The internal reservoir, located under the target vessel, holds 36 litres. There are two thermal links between this reservoir and the target vessel (see figure 9). The first link is a conduction path provided by flexible bundles of thick copper wires thermally anchored to a hollow copper cooling flange (‘heat exchange ring’) attached to the underside of the target vessel. The flexibility helps decouple acoustic/mechanical noise in the LN2 reservoir from the LXe chamber. The other end of the bundle dips into the liquid nitrogen and the thermal impedance depends on the depth of the liquid. The bundle is welded and polished at both ends for good thermal matching. A second thermal path is provided by a direct connection between the nitrogen reservoir and the hollow cooling flange. This allows liquid or boil-off gas to be used as additional coolant and provides the means for active thermal control with minimum cryogen usage, which is important during stand-alone operation underground.

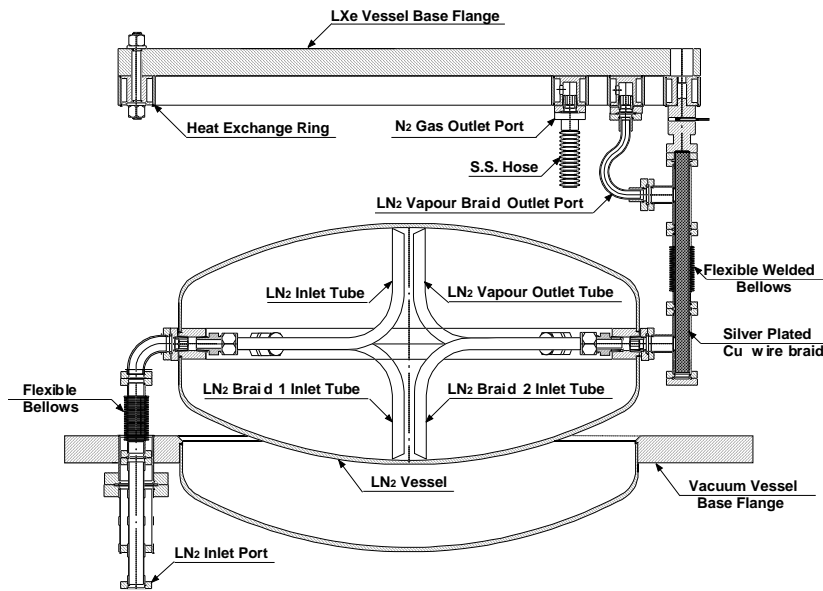


Fig. 9. Thermal control system elements.

Three external pipes are connected to the cooling system. The first is the liquid nitrogen delivery line and this terminates inside the reservoir close to the top. A second pipe also opens to the top of the reservoir, whilst a third pipe connects to the delivery to the cooling flange. The last two pipes are fitted with control valves which regulate the internal pressure and the flow rate through

the hollow cooling flange. During initial cool-down the flow through the cooling flange is increased to allow bulk liquid flow into it. Once cold, the gas flow through the cooling flange provides a fine temperature control mechanism whilst the copper cable bundles provide the main thermal link balancing the average heat load. The heat load is reduced by the use of thermal insulation around both the target vessel and the nitrogen chamber (see figure 10). The nominal operating temperature is around -100°C and the heat load is, as expected, $\sim 40\text{ W}$, giving a design hold-time between refills of ~ 2 days.

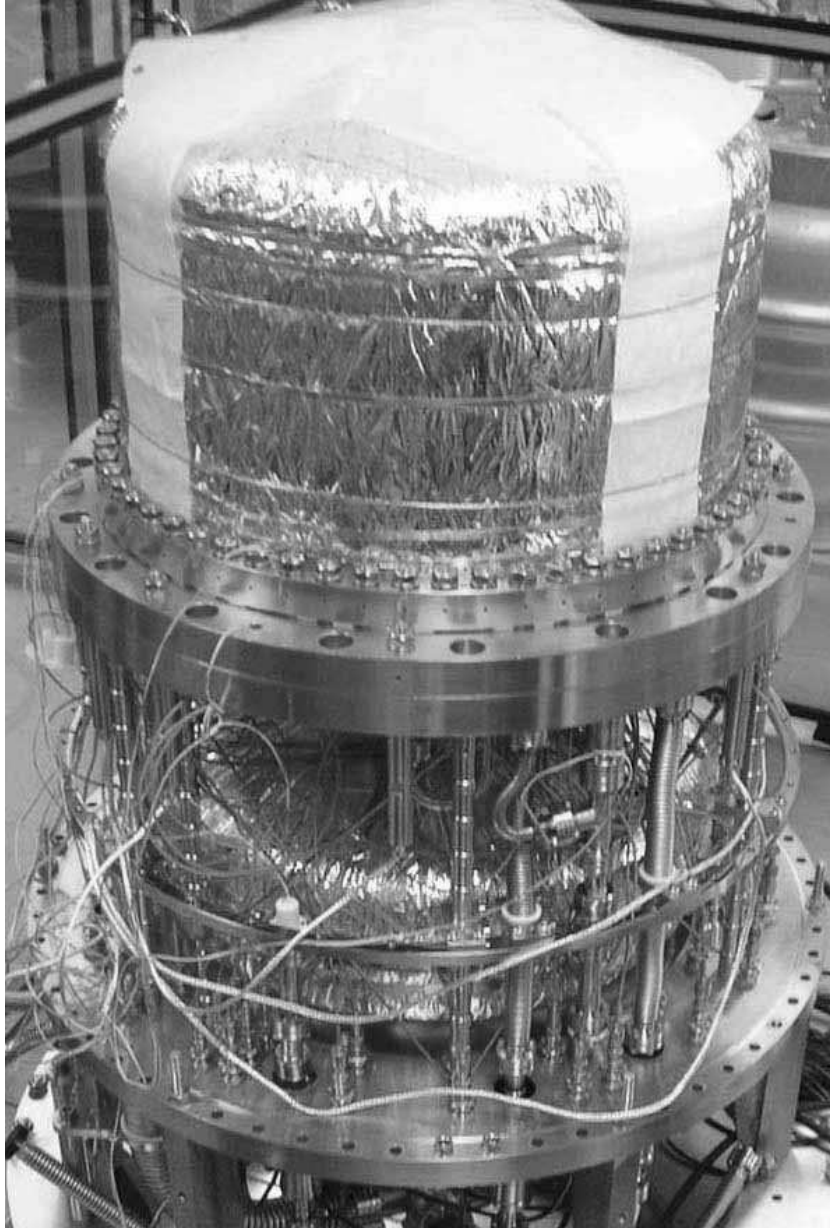


Fig. 10. The assembled instrument without its vacuum jacket giving a view of the target vessel (top) and liquid nitrogen reservoir both covered with thermal insulation.

5 The outer vacuum jacket

The design principles for the vacuum jacket were much the same as for the target vessel, except that the pressure rating was reduced to 4.3 bar absolute. The safety standard for pressure vessels dictated the material thicknesses and process standards and the same attention to background and cleanliness was imposed. Hence OFHC copper was used, with electron beam welding and minimisation of the number of seams; the cylindrical section of this larger vessel was also made from just one rolled plate. The bottom flange has an included domed section and the vacuum seals were all done in the same way as for the target vessel. Figure 11 shows the underside view of the bottom flange.



Fig. 11. The bottom flange of the vacuum jacket showing the inner domed section and the arrangement of feedthroughs and ports around the outer skirt.

6 The gas purification system and safety reservoirs

Figure 12 shows a schematic of the xenon gas purification system. The main requirement is to be able to remove electronegative contaminants which will prevent the ionisation electron drift and suppress the secondary signal. Typically this requires liquid xenon purity down to the parts per billion level, beyond that available through commercial purchase. In addition the level of radioactive krypton needs to be kept as low as possible as the beta-decay of ^{85}Kr gives a continuum energy deposit down into the level expected from

elastic scattering of WIMPs. An all-metal bakeable gas system has been used. The system is pumped by a combination of oil-free scroll and turbo-molecular pumps. The xenon gas is contained in two large stainless steel cylinders fitted with high purity all-metal UHV valves and regulators. These two cylinders stand in cooling jackets allowing them to be cooled to liquid nitrogen temperatures. Two SAES[19] getters are used. Fine particle filters ($0.5 \mu\text{m}$) are fitted to all gas delivery lines. The gas system is fitted with a mass spectrometer which is used both for helium leak testing and residual gas analysis. The base vacuum attainable in the system is $\sim 10^{-8}$ torr, dominated by H_2 ; a partial H_2O pressure of $\sim 10^{-10}$ torr was achieved prior to the xenon input. The detector itself is connected without valves to a port on the main volume of the gas purification system. Another port is connected to the large volume safety reservoirs with only a burst disk between them. This is not only to guard against the safety risk associated with catastrophic failure of the target vessel under overpressure, but also to avoid loss of xenon. The two gas cylinders contain 50 kg of xenon supplied by ITEP from stock collected from underground sources between 20 and 40 years ago. This xenon is expected to have a very low radioactive krypton content. A final component of our gas purification system is a novel portable chamber for electron lifetime measurements which will be described elsewhere[20].

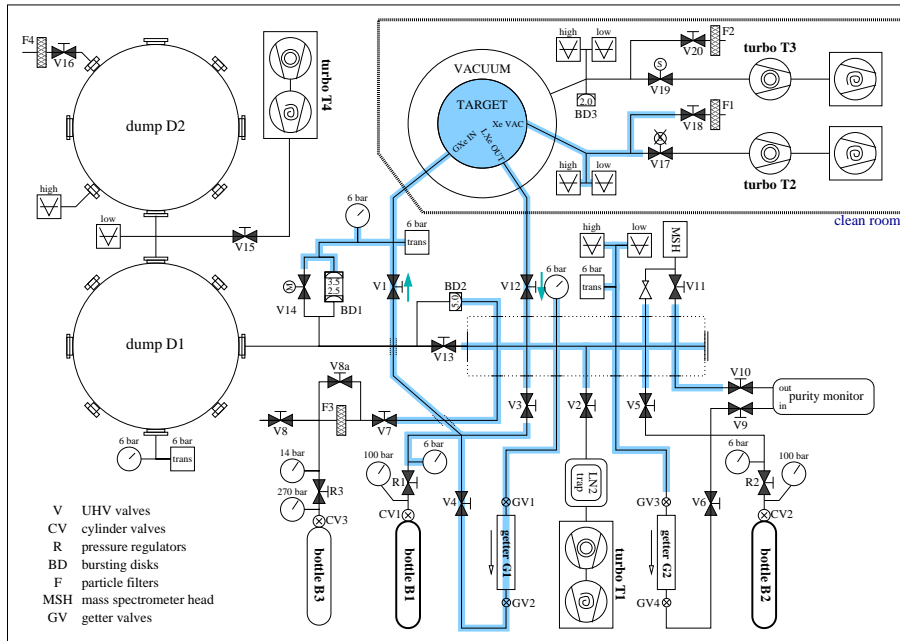


Fig. 12. Schematic diagram of the gas purification system.

7 The data acquisition system

The 31 PMT signals are fed into wideband amplifiers and split into a dual dynamic range data acquisition system (DAQ). This ensures sensitivity to very small primary scintillation signals containing only a few photoelectrons (phe) as well as to large secondaries without saturation. All 62 channels are sampled at 500 MS/s by 8-bit AQIRIS digitisers. For the collection of ‘dark matter’ data a PMT gain of 2×10^5 will be used. Such a low gain should avoid internal PMT saturation effects following very large secondary scintillation signals. Wideband amplifiers add electronic gain in two stages. The first stage is (x10) with a noise referred to the input of $30 \mu\text{V rms}$. They then feed into adjustable attenuators which are used to equalise the single photoelectron response for each PMT. The outputs from this stage then feed into the 31 low-gain digitisers as well as into the next stage x10 wideband amplifiers. The high and low-gain input channels thus have a factor of 10 gain difference which can be further expanded by adjusting the full-scale ranges on the digitisers. A simple threshold trigger signal is derived from a summing amplifier, with inputs from all PMTs, fed into a discriminator whose output provides an external trigger for the AQIRIS digitisers. This trigger can not differentiate between primary and secondary scintillation signals. A more sophisticated trigger using a time to amplitude converter can provide a width measure and differentiate the very short primary scintillation signals ($\sim 30 \text{ ns}$ time constant) from the much more extended secondary scintillation signals ($\sim 1 \mu\text{s}$ duration). The maximum delay between primary and secondary scintillation signals in ZEPLIN III is $\sim 17 \mu\text{s}$. A LINUX-based software application reads out the digitiser crates. A FIFO-type memory buffer, accessed independently by two CPUs for data transfer and write-out, reduces the overall dead time. An acquisition rate of 100 events/s can be sustained.

8 Commissioning cool-down tests

The first cool-down test was designed to verify the thermal control system and to test out the PMT array. For this test the anode and cathode electrodes were replaced by a copper plate located just 8 mm above the PMT array. 31 ^{241}Am radioactive sources were vacuum-sealed into this plate with a thin copper foil overlay to prevent leakage of radioactivity and to stop α -particles from interacting in the xenon. These then provided a source of low-energy (mainly 59.6 keV) photons. For subsequent cool-down tests the radioactive sources had been removed and the full electric field system installed in its final configuration.

8.1 Cooling system

The cooling system performance during the first cool-down was as expected. The initial cool-down period used 200 litres of liquid nitrogen and progressed at $\sim 5\text{ }^\circ\text{C}/\text{hour}$. An array of temperature sensors was used to monitor critical points within the instrument. One of these, on the lower face of the cooling flange on the bottom of the target, is used as the control temperature and its reading is compared with a set temperature in the controller to automatically operate two valves: one which exhausts straight from the gas volume of the nitrogen reservoir, and one which exhausts through the cooling ring. Once down at the nominal operating temperature ($\sim -100\text{ }^\circ\text{C}$) the temperature of the target vessel is stable to better than 0.2°C and the liquid nitrogen usage drops to $\sim 20\text{ litres}/\text{day}$ as expected. Figure 13 shows some key engineering parameters monitored over a 24 hour period during the second cool-down test. The upper trace is from the temperature sensor on the cooling flange and the periodic behaviour is due to the control system. The lower trace is then the temperature of the base plate of the target vessel itself.

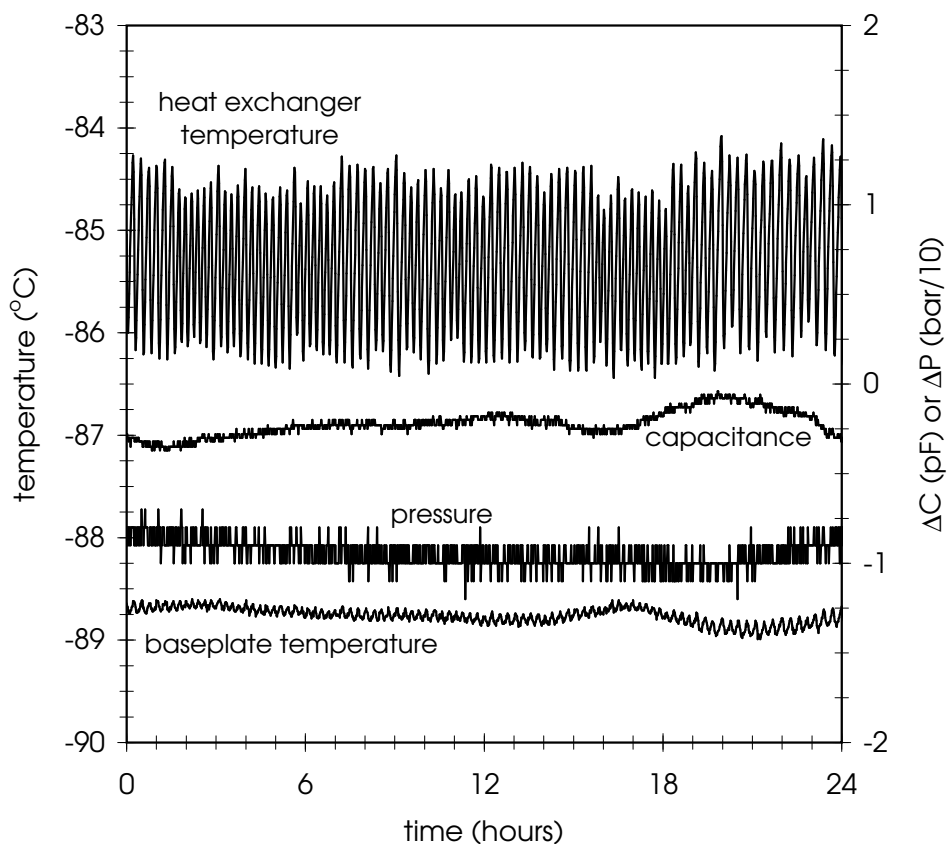


Fig. 13. Some key system engineering parameters monitored over a 24 hour period.

8.2 PMT array

Pulse height spectra, pulse waveforms and single photoelectron spectra were collected from all PMTs during the first cold-run both with the DAQ electronics just described and with a pulse height analysis (PHA) set-up using a multichannel analyser (MCA). These confirmed correct operation of all 31 PMTs in the array, including ~ 1000 crimped connections! A typical primary scintillation pulse from a 59.6 keV photon interaction is shown in figure 14. This shows the characteristic decay time of ~ 40 ns. The single photoelectron spectra show well resolved peaks and these were used to set the amplifier gains in order to normalise all channels to the same overall gain.

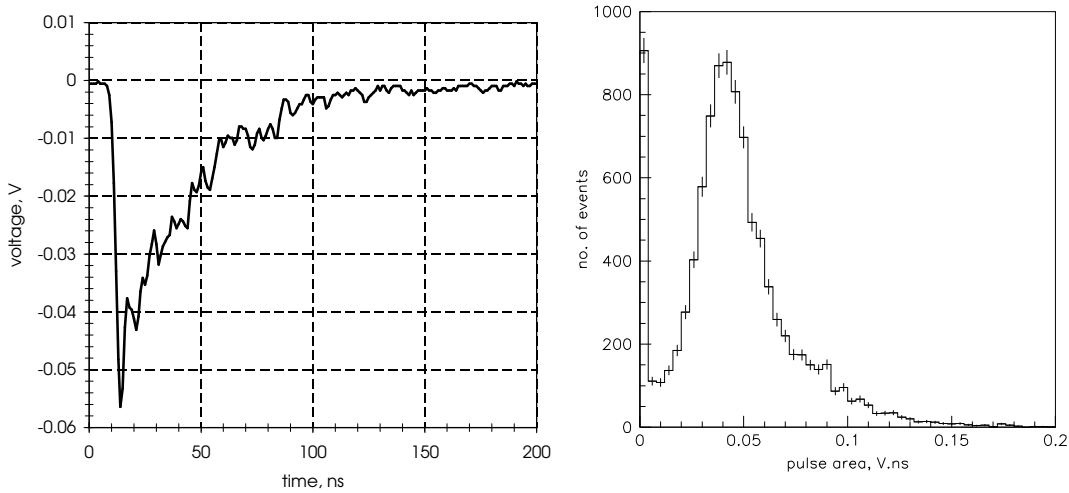


Fig. 14. A typical primary scintillation pulse from a 59.6 keV photon interaction and a single photoelectron spectrum from one of the PMTs. Both the spectrum and the scintillation pulse were obtained with +2kV on the PMT anode; however there was an additional $\times 10$ amplifier present for the spe measurement.

8.3 Scintillator performance

LXe scintillates in the vacuum ultraviolet (VUV), near 175 nm, with a yield comparable to the best scintillator crystals. The VUV luminescence is produced by the decay of singlet and triplet states of the Xe_2^* excimer. These can be formed directly by excited atoms left by the interacting particle or as a result of recombination into an excited state along the particle track [21,22].

Figure 15 shows a typical spectrum taken from one PMT when the internal ^{241}Am sources were in place. The plot shows two spectra. The bottom spec-

trum was taken with the whole arrangement covered with liquid xenon. The two spectral features are the 59.6 keV line from ^{241}Am and a blend of the 26.3 keV ^{241}Am γ -ray with a 30 keV line resulting from escape of Xe K-shell fluorescence photons. Using the measured single photoelectron spectrum from this PMT gives a signal level of ~ 12 phe/keV. For this measurement there is no applied electric field. The top spectrum was taken with the liquid level between the source and the PMT window. The interaction occurred in the liquid phase and the improved light collection (up to ~ 17 phe/keV is a result of total internal reflection at the liquid gas interface due to the refractive index mismatch. The resolution from the two-phase spectrum is $\sim 13\%$ FWHM. More detailed and extensive physics results from the first cold run will be published separately[23].

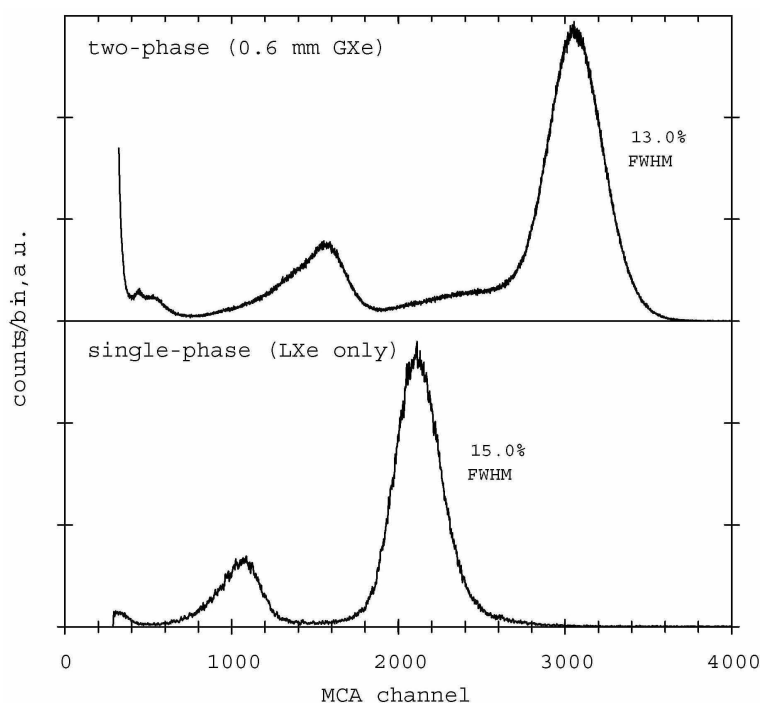


Fig. 15. Pulse height spectra obtained from the ^{241}Am primary scintillation signals during the first cool-down test. The two panels correspond to two different liquid xenon levels. The highest energy peaks in both spectra are at 59.6 keV.

8.4 Two-phase operation

Once the radioactive sources used for the measurements in the previous section had been removed the second and subsequent cold-runs have successfully loaded the detector with liquid xenon. A capacitive level-sensing system probes the liquid xenon height with sub-mm accuracy at three locations in the chamber. A signal from one of these coaxial capacitor structures, readout to 0.03 pF

accuracy, is shown in figure 13. In underground operation, these sensors will be integrated with an active levelling system in order to maintain the electrodes parallel to the liquid surface, guarding the heavily shielded detector against any structural deformation of the underground cavern.

With the xenon filled to its nominal depth, but with no applied electric field, figure 16 shows ^{57}Co spectra obtained with an external uncollimated source placed above the detector. Two spectra are shown, both reconstructed using the outputs from all the PMTs. The shaded one, however, only includes events in which the peak signal occurred in one of the inner seven PMTs. This ‘collimated’ spectrum has a FWHM of $\sim 25\%$, which we expect will improve once final corrections for PMT sensitivities are done. The broad shoulder on the low side for the uncollimated spectrum is purely due to light collection variation towards the edge of the xenon volume (way outside the fiducial volume).

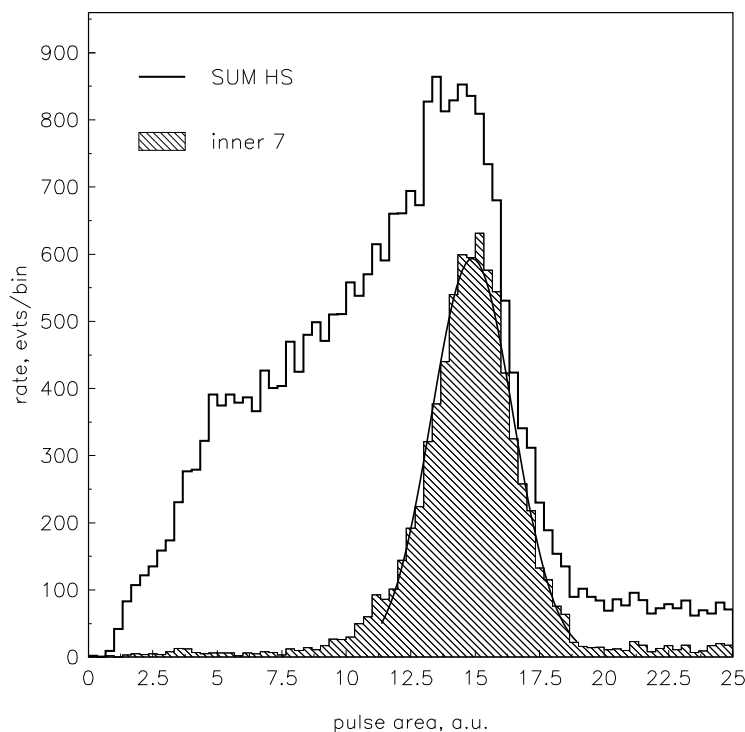


Fig. 16. Pulse height spectra obtained from using an external ^{57}Co source above the instrument.

After the zero-field tests, 13.5 kV were applied between the cathode grid and the anode mirror, setting up a field of 3.0 kV/cm in the liquid. Figure 17 shows a typical signal from a γ -ray interaction in the liquid. The fast scintillation is the primary signal, S1, caused by direct excitation created by the photoelectron. The second, broader signal, S2, occurs when the ionisation also created has drifted to the liquid surface and has been extracted into the gas phase. Once in the gas phase the electric field is strong enough to cause excitation leading to a burst of additional photons. The time delay depends on the depth

at which the interaction happened and the drift velocity at our operating fields is $\sim 2.5 \text{ mm}/\mu\text{s}$. The width of the secondary depends on the gas gap and the electric-field in the gas. The secondary emission shows a flat plateau as the charges drift across the gap. The rise and fall time is due to a combination of extraction dynamics, diffusion and the gas scintillation time-constant. The ratio of the two areas (S2/S1) is ~ 150 as expected at this field.

One of the key design drivers of ZEPLIN-III was the ability to resolve each interaction point in the three dimensions. A position reconstruction algorithm was developed from simulated datasets which will provide sub-cm resolution in the horizontal plane [24]. Even before this is applied to real data, this spatial sensitivity is well demonstrated in figures 18 and 19, showing an event in which two interactions have overlapped in time. Moreover there are at least four secondary signals. Without position sensitivity it would not be possible to separate these two events just from the summed signals. However, looking at the individual PMT traces (left-hand panel in figure 19) it is immediately obvious that these two events have happened in very different parts of the detector (right-hand panel) and they can be unambiguously separated. They are both double-Compton scatters.

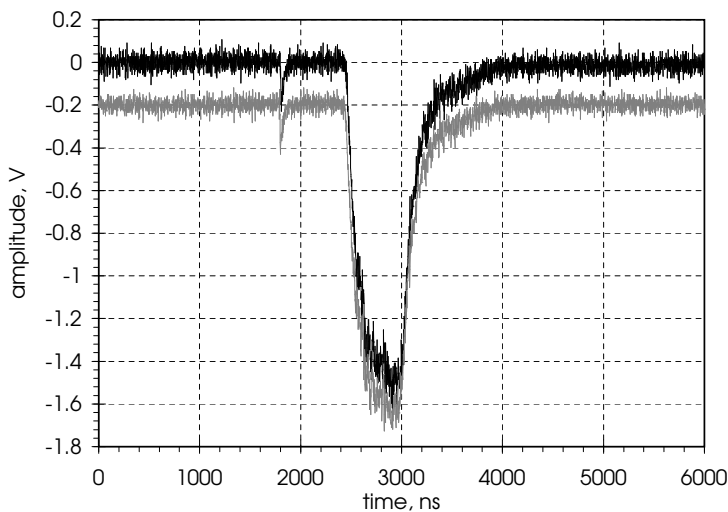


Fig. 17. Summed waveforms from a γ -ray event showing a fast primary pulse followed by the secondary wider pulse from electroluminescence in the gas phase caused by ionisation drifted from the event site. The two traces shown are from the dual range DAQ. The low-sensitivity data have been multiplied by 10.

9 Summary

The key design features of the ZEPLIN III instrument have been described. The challenging and pioneering aspects of the manufacturing technologies and

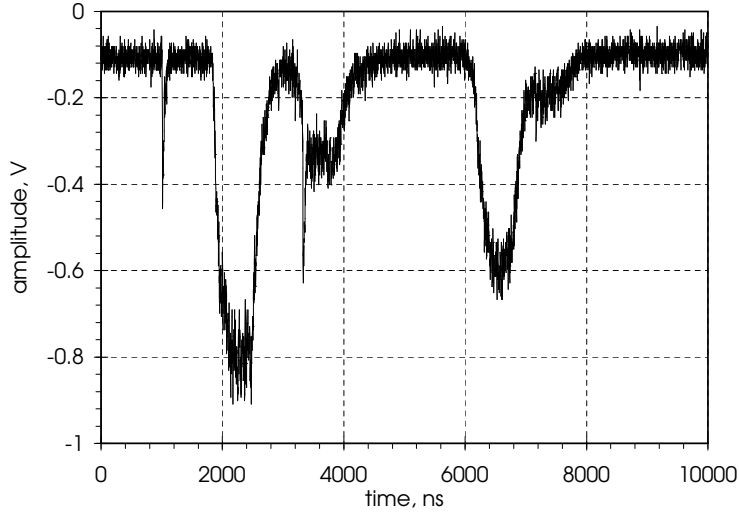


Fig. 18. Summed waveforms from two overlapping γ -ray events both showing fast primary signals followed by secondary signals.

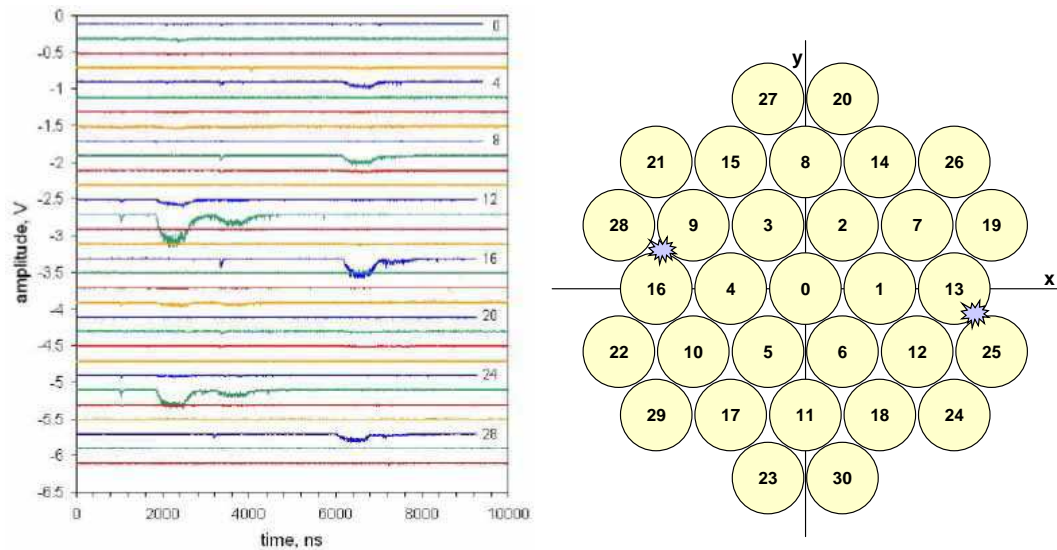


Fig. 19. Individual waveforms from the 31 PMTs showing how the two overlapping events can be separated using position reconstruction. The reconstructed positions are indicated on the right-hand panel and the size of the symbols is representative of the position resolution.

procedures have been detailed and first commissioning data have been presented to demonstrate the successful completion of build of this instrument. Further extensive calibration work is now needed to prepare this instrument for use as a dark matter detector. To fully characterise ZEPLIN III much of this will need to be done underground in a lower background environment.

10 Acknowledgements

This work has been funded by the UK Particle Physics And Astronomy Research Council (PPARC). We would like to acknowledge the superb copper machining achieved within the Imperial College Physics Department workshop led by R. Swain, and the development of new welding techniques by The Welding Institute.

References

- [1] T. J. Sumner (2005), *New Astronomy Reviews* **49**, 277–281.
- [2] H. M. Araújo (2005), *Proc. Int. Conf. Dielectric Liquids*, Coimbra, Portugal, IEEE Press (IEEE Cat. 05CH37643), 305.
- [3] G. J. Alner *et al.* (2005), *New Astronomy Reviews* **49**, 259–263.
- [4] G. J. Alner *et al.* (2005), *Nucl. Instrum. Meth.* **A555**, 173–183.
- [5] B. A. Dolgoshein, V. N. Lebedenko & B. U. Rodionov (1970), *JETP Lett.* **11**, 513
- [6] T. J. Sumner *et al.* (1999), *Proc. 26th Int. Cosmic Ray Conf.*, **2**, ed. D. Kieda, M. Salamon & B. Dingus, 516.
- [7] A. S. Howard *et al.* (2001), *Proc. 3rd Int. Workshop on the Identification of Dark Matter*, ed. N. J. C. Spooner & V. Kudryavtsev, Singapore: World Scientific, 457.
- [8] D. Yu Akimov *et al.* (2003), *Proc. 4th Int. Workshop on the Identification of Dark Matter*, ed. N. J. C. Spooner & V. Kudryavtsev, Singapore: World Scientific, 371.
- [9] D. Davidge (2003), PhD Thesis, University of London.
- [10] J. Dawson (2003), PhD Thesis, University of London.
- [11] H. M. Araújo *et al.* (2006), *Astropart. Phys.* accepted. (arXiv:astro-ph/0603243)
- [12] E. Aprile *et al.* (2006), (ArXiv: astro-ph/0601552)
- [13] H. M. Araújo *et al.* (2004), *Nucl. Instrum. Meth.* **A521**, 407–415.
- [14] N. J. T. Smith *et al.*, in preparation.
- [15] ANSYS Inc. (www.ansys.com)
- [16] CRC Handbook of Chemistry & Physics, pp. 12-120
- [17] <http://www.twi.co.uk/>

- [18] <http://www.alconox.com>
- [19] <http://www.saesgetters.com/>
- [20] R. Walker et al. in preparation
- [21] S. Kubota *et al.* (1979), *Phys. Rev. B* **20(8)**, 3486–96.
- [22] A. Hitachi *et al.* (1979), *Phys. Rev. B* **27(9)**, 5279–85.
- [23] V. Chepel, C. Thorne *et al.* (2006), in preparation.
- [24] A. Lindote *et al.* (2005), *Nucl. Instrum. Meth. A*, *in press*.